Surface acoustic wave effect on magnetic domain wall dynamics

Jintao Shuai,[1] Luis Lopez-Diaz,[2] John E. Cunningham,[3,*] and Thomas A. Moore[1,†]
[1]*School of Physics and Astronomy, University of Leeds, Leeds LS2 9JT, United Kingdom*
[2]*Department of Applied Physics, Universidad de Salamanca, Salamanca E-37008, Spain*
[3]*School of Electronic and Electrical Engineering, University of Leeds, Leeds LS2 9JT, United Kingdom*

(Received 26 June 2023; revised 11 September 2023; accepted 12 September 2023; published 26 September 2023)

Surface acoustic waves (SAWs) have significant potential for the energy-efficient control of magnetic domain walls (DWs). This study investigates the influence of SAW frequency (50, 100, and 200 MHz) on DW dynamics in magnetic thin films. Micromagnetic simulations are performed to examine the effects of SAWs on DW velocity. The results demonstrate that SAWs enhance DW motion by promoting the depinning of DWs from pinning sites through SAW-induced spin rotation. This spin rotation exhibits the same frequency as the applied SAWs. The impact of SAW frequency varies depending on the level of anisotropy disorder in thin films. In films with 3% anisotropy disorder, the DW velocity increases with SAW frequency, highlighting the amplifying effect of spin rotation and enhanced DW depinning. Conversely, in thin films with 1% anisotropy disorder, the DW velocity decreases with SAW frequency owing to significant SAW-induced energy dissipation via spin rotation. These findings underscore the intricate interplay between SAWs, spin rotation, and DW dynamics, emphasizing the role of anisotropy disorder in governing the response of DWs to SAWs. The study contributes to the understanding of SAW-assisted DW motion and provides insights into the optimization of and energy-efficient control of DWs in spintronic applications using SAWs.

DOI: 10.1103/PhysRevB.108.104420

I. INTRODUCTION

Magnetic domain wall (DW) motion in thin films with perpendicular magnetic anisotropy (PMA) shows potential for technological applications in spintronics, such as magnetic racetrack memory and logic devices [1–7]. DW motion can be induced by an external magnetic field through two distinct mechanisms. In an ideal thin film without any defects or disorder, when subjected to low fields, the DW velocity increases with the field strength, which is accompanied by a slight distortion in the wall structure. Above a threshold ($\mathbf{H}_{\mathrm{W}}$), DW velocity experiences an abrupt decrease with the field. This phenomenon is widely recognized as Walker breakdown, characterized by an alternating DW structure and the precession of magnetization inside the DW around the applied field [8].

Defects and disorders within thin films significantly influence the DW motion. In a thin film containing such imperfections, at zero temperature, the DW becomes strongly entangled with the defects and remains pinned for all fields below a critical value known as the depinning field ($\mathbf{H}_{\mathrm{dep}}$). The depinning field is defined as the minimum external magnetic field required to surpass the local energy barrier that hinders the DW motion [9,10]. At finite temperatures, DW motion can be activated by thermal fluctuations, which initiate localized depinning process. This regime is commonly referred to as the creep regime, where DW velocity increases with the external magnetic field and follows the creep law [11–13]. This behavior holds even when the applied field is smaller than the $\mathbf{H}_{\mathrm{dep}}$. For fields exceeding $\mathbf{H}_{\mathrm{dep}}$ at both temperature conditions, the DW velocity increases with the field until it enters the viscous regime where the DW velocity exhibits a wide plateau [14–17] instead of a Walker breakdown. This DW velocity saturation effect can be attributed to an enhanced energy dissipation at defects in the thin film [16], as well as the blocking [18] and annihilation [19] of vertical Bloch lines (VBLs).

VBLs are curling magnetic structures that appear inside DWs; they introduce complexity into the static and dynamic properties of the DWs [20,21]. Defects within thin films give rise to variations in the energy landscape along the DW, which in turn affect the wall structure and the local mobility of the DW as it traverses its path. The DW structure thus directly influences the local mobility. As a result, the nucleation, propagation, and annihilation of VBLs have a significant impact on the overall DW dynamics.

Surface acoustic waves (SAWs) are elastic waves that propagate along the surface of a piezoelectric material, and are capable of introducing dynamic strain waves into magnetic thin films [22]. Through the magnetoelastic coupling effect, these dynamic strain waves generate a dynamic energy landscape, thereby triggering magnetization precession [23–25], facilitating magnetization switching [26,27], and enhancing the DW motion [28–33]. For instance, Dean *et al.* presented theoretical evidence that standing SAWs can solely drive DW motion and create pinning sites remotely due to the SAW-induced strain gradient. They demonstrated that by adjusting

*Corresponding author: j.e.cunningham@leeds.ac.uk
†Corresponding author: t.a.moore@leeds.ac.uk

the SAW frequency, multiple DWs can be synchronized and moved simultaneously [28]. Edrington *et al.* conducted experimental investigations showing that standing SAWs effectively drive DW motion from the creep regime to the flow regime in Co/Pt multilayers [29]. Adhikari *et al.* explored the impact of SAWs on enhancing DW motion within the creep regime by the SAW-induced effective field and increasing the likelihood of DW depinning [34,35].

SAWs have demonstrated significant promise for achieving energy-efficient control of DW motion. However, a comprehensive understanding of the detailed mechanisms and effects underlying the interaction between SAWs and DWs is currently lacking. Moreover, the influence of defects and disorders in thin films on SAW-assisted DW motion remains largely unexplored. Thus, there is a knowledge gap regarding the systematic investigation of the impact of SAW frequency on DW dynamics in films with varying levels of disorders. Addressing this gap is crucial for advancing our understanding of SAW-assisted DW motion and unlocking its full potential for energy-efficient DW control.

In this study, we investigate the influence of SAW frequency (50, 100, and 200 MHz) on DW motion within thin films with different levels of anisotropy disorder (1% and 3%) at low fields (up to 1 mT) using micromagnetic simulations. This study also delves into the DW depinning process under different conditions, with a particular focus on VBLs. By conducting these investigations, we aim to gain insights into the intricate dynamics of SAW-assisted DW motion and its interaction with disorder, ultimately contributing to the development of energy-efficient DW control techniques.

II. MODEL AND COMPUTATIONAL DETAILS

Figure 1(a) depicts a schematic diagram of the proposed device that could be implemented by forming a Pt/Co/Pt microwire with PMA deposited onto a 128° Y-cut lithium niobate, for example. At both ends of the magnetic thin film, a pair of interdigitated transducers (IDTs) are patterned. By adjusting the width and pitch of the IDT electrodes, SAWs with various frequencies can be generated. Figure 1(b) shows the simulated system employed in this study. The simulations in this paper are performed using Mumax3, a GPU-accelerated micromagnetic simulation program [36]. Mumax3 integrates numerically the Landau-Lifshitz-Gilbert equation

$$\frac{d\mathbf{M}}{dt} = -\gamma \mathbf{M} \times \mathbf{H}_{\text{eff}} + \frac{\alpha}{M_s}\mathbf{M} \times \frac{d\mathbf{M}}{dt}, \tag{1}$$

where $\mathbf{M}$ is the magnetization vector, M_s is the saturation magnetization, t is the time, γ is the gyromagnetic ratio, $\mathbf{H}_{\text{eff}}$ is the effective magnetic field acting on the magnetization, and α is the Gilbert damping constant. A Bloch DW separating the left and right domains is initialized at a distance of one-fourth from the left edge. The system then relaxes to equilibrium before an external magnetic field ($\mathbf{H}_{\text{ext}}$) pointing "in" was applied favoring the DW motion towards the right. The dynamics of the DW is simulated for 100 ns. The material parameters used in the simulations were chosen to match those of the Pt/Co/Pt thin films [37]: saturation magnetization $M_s = 6 \times 10^5$ A/m, exchange constant $A_{\text{ex}} = 1.0 \times 10^{-11}$ J/m, anisotropy constant

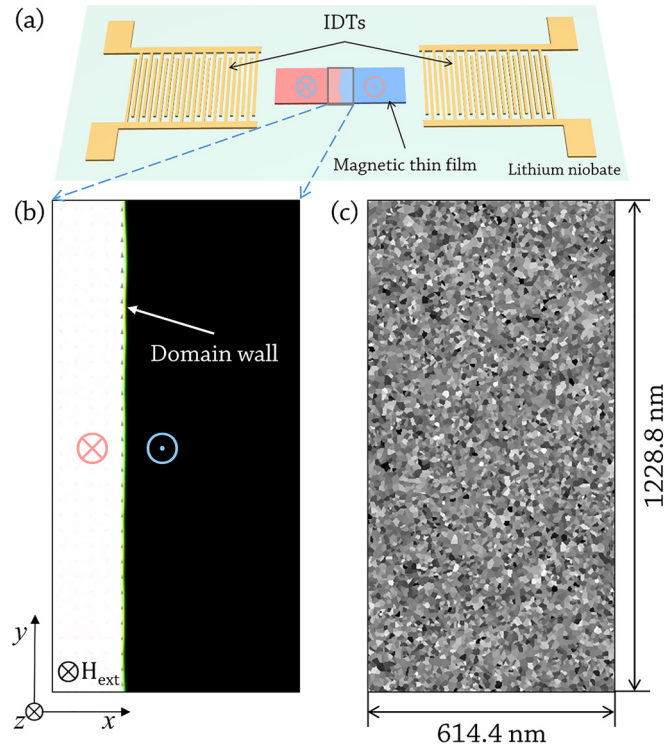

FIG. 1. (a) Schematic diagram of the proposed device (not to scale). A magnetic microwire with perpendicular magnetic anisotropy is deposited onto a lithium niobate substrate. A pair of IDTs, which can be used to launch SAWs, are fabricated at opposite ends of the microwire. (b) Initial magnetization of the microwire (with dimensions of $614.4 \times 1228.8 \times 1$ nm^3). Bloch DW separates the left and right domains. The external magnetic field pointing in plane was applied, favoring the expansion of the left domain. The traveling SAWs propagate from left to the right along the x axis. (c) A typical grain distribution is shown, where the grey level is proportional to the value of perpendicular magnetic anisotropy K_u for each grain.

$K_u = 8 \times 10^5$ J/m^3, and Gilbert damping constant $\alpha = 0.01$. The grid size and cell size of the simulation are $256 \times 512 \times 1$ nm^3 and $2.4 \times 2.4 \times 1.0$ nm^3, respectively, which result in a computational region of $614.4 \times 1228.8 \times 1$ nm^3. To isolate the SAW-induced effects from the temperature, simulations were performed at 0 K unless otherwise specified.

To introduce disorder in our simulations, we utilize the built-in function of Mumax3, which defines grain-like regions using Voronoi tessellation [38]. A typical grain distribution with an average diameter $d = 10$ nm is shown in Fig. 1(c) [16,39]. We assign anisotropy constants (K_u) to each grain, randomly distributed according to a normal distribution centered around their nominal value of 8×10^5 J/m^3. The standard deviation (σ) is utilized to control the level of disorder. Specifically, we consider two typical values of σ: 1% and 3% [16,40,41]. A higher σ indicates a greater variation in the anisotropy constants within the thin film, resulting in a higher pinning energy and enhanced pinning effects. By manipulating the σ value, we can effectively modulate the degree of disorder and its impact on the magnetic behavior of the system during simulations.

The magnetoelastic coupling effect is implemented using Mumax3 built-in module [42]. The magnetoelastic energy density (E_{me}) in the system can be described by

$$E_{\text{me}} = B_1 \sum_{i=x,y,z} m_i^2 \varepsilon_{ii} + B_2 \sum_{i \neq j} m_i m_j \varepsilon_{ij}, \tag{2}$$

where B_1 and B_2 represent the magnetoelastic coefficients, ε_{ij} denotes the strain tensor, $m_{i,j}$ are the normalized magnetization, $m = M/M_{\text{s}}$, and i, j are Cartesian components (x, y, z). The effective field ($\mathbf{H}_{\text{eff}}$) can be expressed as the first derivative of the total energy density with respect to the magnetization, given by

$$\mathbf{H}_{\text{eff}} = -\frac{1}{\mu_0 M_{\text{s}}} \frac{\delta E}{\delta \mathbf{m}}, \tag{3}$$

where μ_0 is the permeability of vacuum and E represents the free energy density of the system. The effective field introduced by the magnetoelastic interaction can thus be expressed as

$$\mathbf{H}_{\text{me}}^{(i)} = -\frac{2}{\mu_0 M_{\text{s}}} \left(B_1 m_i \varepsilon_{ii} + B_2 \sum_{j:j \neq i} m_j \varepsilon_{ij} \right), \tag{4}$$

where $\mathbf{H}_{\text{me}}^{(i)}$ is the component of the effective field along the axis labeled by i. It should be noted that the film is considered acoustically thin, meaning that it is sufficiently thin and rigid for the chosen SAW frequency [43]. As a result, only the in-plane strain component (ϵ_{xx}) needs to be taken into account [28,37,44]. In our simulations, we set B_1 to be 1.5×10^7 J/m^3, and $B_2 = 0$. To implement the traveling SAW (ϵ_{xx}) within Mumax3, we utilize a space- and time-dependent strain tensor as follows:

$$\epsilon_{xx} = A(\sin(\omega t)\cos(kx) - \cos(\omega t)\sin(kx)), \tag{5}$$

where k and ω represent the wave number and angular frequency of the SAW, respectively. $A = 0.006$ denotes the amplitude of the SAW. The velocity of SAWs propagating in lithium niobate is reported as 4000 m/s [45].

The velocity of the DW, denoted as v, is determined by the change in the average normalized magnetization along the z axis ($\Delta\langle m_z \rangle$) and can be expressed as

$$v = \frac{L_x \Delta\langle m_z \rangle}{2\Delta t_s}, \tag{6}$$

where $L_x = 614.4$ nm represents the length of the computational region, and $\Delta t_s = 100$ ns is the simulation time. To investigate the effect of SAW frequency on DW dynamics, we set the frequencies of the SAWs as either 50, 100, and 200 MHz. For each value of the applied field the magnetization is set to initial magnetization. To account for the variation in depinning energy among different samples, we generate 10 stochastic realizations for each frequency and disorder level, using the same material parameters but different grain distributions. The data points presented in the results are the ensemble averages of these 10 stochastic realizations, along with corresponding error bars, which indicate the ensemble spread of the 10 simulations.

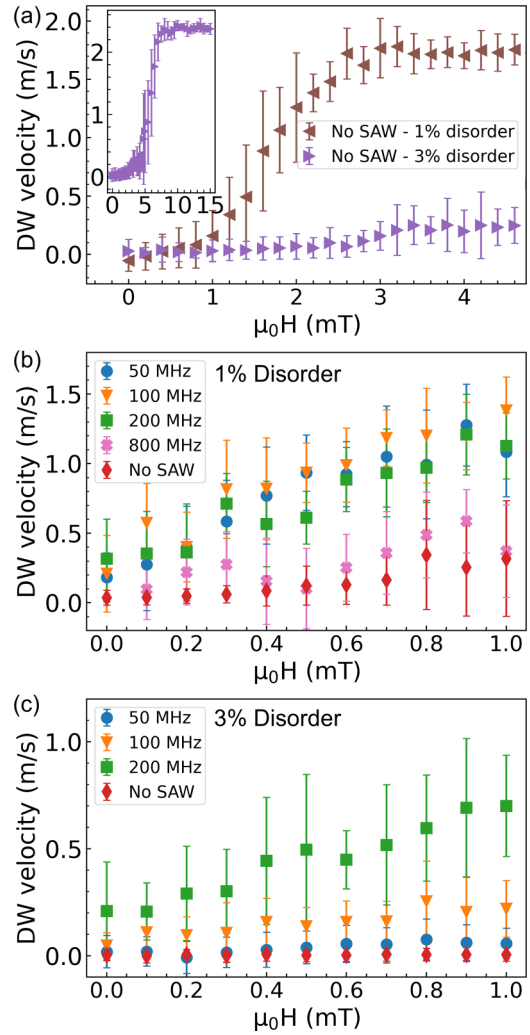

FIG. 2. (a) DW velocity as a function of the applied external magnetic field from 0 to 4.6 mT without SAWs in thin film with 1% and 3% anisotropy disorder. Inset graph shows the DW velocity (y axis, m/s) of the thin film with 3% anisotropy disorder against the applied field (x axis, mT) from 0 to 15 mT. DW velocity as a function of the applied external magnetic field from 0 to 1 mT without SAWs and in the presence of SAWs with frequencies of 50, 100, and 200 MHz in thin film with (b) 1% and (c) 3% anisotropy disorder. Error bars represent the ensemble spread of 10 simulations.

III. RESULTS AND DISCUSSION

Figure 2 shows the DW velocity as a function of the external magnetic field. For the thin film with 1% anisotropy disorder, DW velocity gradually increases with increasing external magnetic field [see Fig. 2(a)], which can be attributed to the relatively low level of anisotropy disorder. Following this, the DW velocity experiences a rapid increase as the field strength rises from 1 to 3 mT. Eventually, a plateau is reached where the DW velocity depends very litter on the external magnetic field. The emergence of the plateau in thin film with disorder has been investigated in previous studies [16,46,47]. For thin films with 3% anisotropy disorder, the DW velocity is almost zero until a higher depinning field of 3 mT is applied.

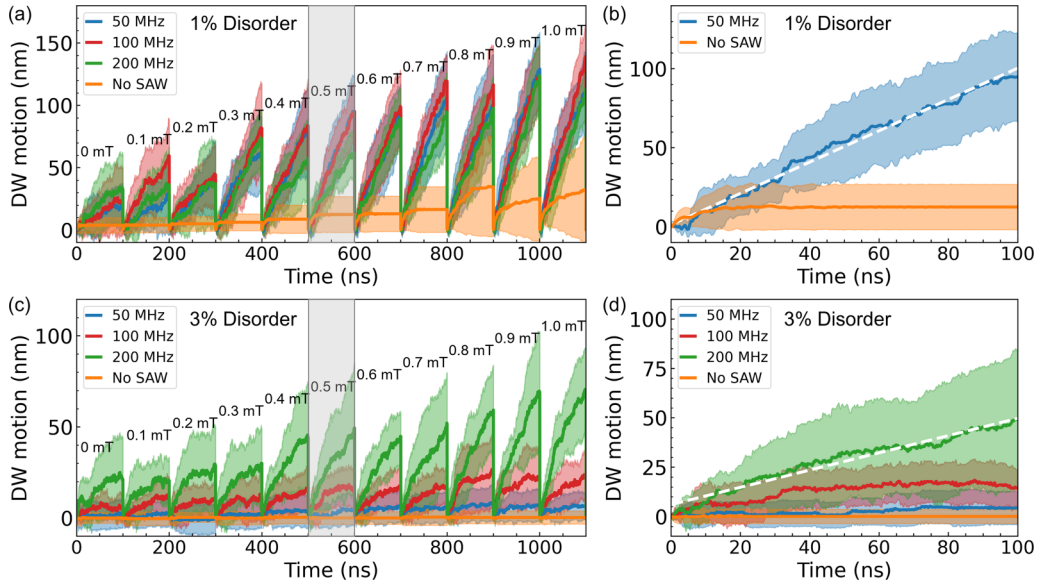

FIG. 3. Time evolution of DW motion in thin films with (a) 1% and (c) 3% anisotropy disorder. DW motion at each applied field is performed for 100 ns, followed by returning to the initial magnetization for the next simulation. Shaded areas represents the ensemble spread of 10 simulations. The applied field for each simulations is labeled. (b) and (d) are zoomed-in views of the enclosed areas in (a) and (c), respectively. The dash lines in (b) and (d) are the linear fits of the corresponding curves.

It enters a plateau at approximately 7 mT [as depicted in the inset graph in Fig. 2(a)].

This study primarily focuses on the motion of magnetic DWs under low magnetic fields (up to 1 mT). At weak applied fields, particularly around the depinning field, the probability of the DW escaping from pinning sites is contingent upon the local energy potential associated with those sites. The magnitude of this energy potential is influenced by material defects, with a specific emphasis on anisotropy disorder in this paper. Notably, the pinning energy exhibits significant variation across different samples. To account for this variation, we perform simulations using 10 stochastic samples, resulting in a broad ensemble spread. In the thin film with 1% anisotropy disorder, and with no SAWs applied, the DW velocity steadily increases from 0.04 ± 0.05 m/s to 0.3 ± 0.4 m/s as the magnetic field rises from 0 to 1 mT [see Fig. 2(b)]. However, the presence of SAWs substantially enhances the DW motion across all studied frequencies. For instance, compared to the case without SAWs, the DW velocity is amplified by a factor of 2.7, reaching 1.1 ± 0.3 m/s with an applied field of 1 mT and 50 MHz SAWs. It is worth noting that the DW velocity gradually decreases with increasing SAW frequency. For example, in the presence of 200 MHz SAWs, the overall trend of the DW velocity curve lies below that observed with 50 MHz SAWs. To further illustrate this effect, we perform simulations with 800 MHz SAWs, and the results show that the DW velocity is significantly slower compared to the velocities observed with SAW frequencies ranging from 50 to 200 MHz.

In the case of the thin film with 3% anisotropy disorder [see Fig. 2(c)], the DW velocity within the studied field range is notably slower compared to the thin film with 1% anisotropy disorder. This difference can be attributed to the higher pinning energy associated with the increased disorder level [13,16]. Within the applied field range of 0–1 mT, the DW velocity shows minimal change due to the depinning field being at 3 mT [as shown in Fig. 2(a)]. However, the introduction of SAWs leads to a significant enhancement in the DW velocity, particularly with the presence of 200 MHz SAWs. Comparing the DW velocity with 1 mT alone to the DW velocity in the presence of 200 MHz SAWs, an increase from 0.004 ± 0.03 m/s to 0.7 ± 0.2 m/s is observed. Interestingly, the DW velocity increases with increasing SAW frequency in the thin film with 3% anisotropy disorder, which is contrary to the observations made in the thin film with 1% anisotropy disorder.

To explore the influence of SAW frequency on the dynamics of DWs in thin films with varying levels of disorder, we examine the DW motion as a function of simulation time, as shown in Fig. 3. For each value of applied field, simulation is conducted for a duration of 100 ns, followed by resetting the initial magnetization before the start of the subsequent simulation. We begin by discussing the thin film with 1% anisotropy disorder in the absence of SAWs. From Fig. 3(a), it is evident that the depinning field of the DW is approximately 0.4 mT in the absence of SAWs. Below this field, no noticeable DW motion is observed. In Fig. 3(b), a more detailed view of DW motion at 0.5 mT is presented. Initially, in the presence of only the magnetic field, the DW moves towards the right for approximately the first 20 ns, followed by a pinning event that persists until the end of the simulation. As the field strength increases, the DW advances more until the DW is pinned at a position for which the depinning field is larger than the applied field. For instance, at external magnetic fields of 0.6, 0.7, and 0.8 mT, the pinning occurs after approximately 30, 35, and 50 ns, respectively.

We further explore the impact of SAWs on DW motion within the same thin film. Even at 0 mT applied field, a significant displacement of the DW is observed when SAWs with frequencies of 50, 100, and 200 MHz are applied. This observation suggests that the introduced SAWs effectively

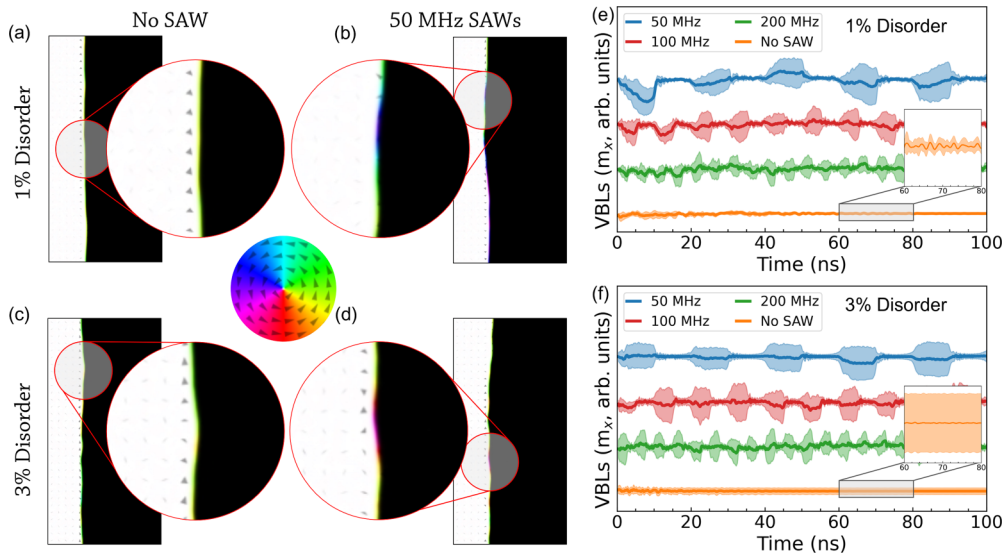

FIG. 4. Snapshots of the magnetization configuration under an applied field of 0.5 mT at 10 ns in thin films with (a) 1% disorder without SAW, (b) 1% disorder with 50 MHz SAWs, (c) 3% disorder without SAW, and (d) 3% disorder with SAWs. Inset graphs in (a)–(d) represent the enlarged magnetization configuration of the corresponding enclosed area. The color code for the in-plane magnetization component is shown by a color wheel. The number of VBLs against the simulation time in thin film with (e) 1% and (f) 3% anisotropy disorder under an applied field of 0.5 mT without SAWs and in the presence of SAWs with frequencies of 50, 100, and 200 MHz. Inset graphs in (e) and (f) are zoomed-in view of VBLs number against simulation time (60–80 ns) without SAWs (two graphs share the same scale). Shaded areas indicate the ensemble spread of 10 simulations. The number of VBLs (y axis) is shifted for clarity of changes.

facilitate DW depinning from pinning sites. Moreover, regardless of the SAW frequency, the DW exhibits continuous motion at a consistent velocity, as indicated by the dashed line overlaying the DW motion curve in Fig. 3(b). The pinning events observed in the absence of SAWs are absent when SAWs are applied, as depicted in Fig. 3(a). Instead, steeper slopes in the DW displacement over time are observed with increasing external magnetic field, indicative of higher DW velocities, as illustrated in Fig. 2(b).

Next, we examine the behavior of the DW in the thin film with 3% anisotropy disorder. Figure 3(c) illustrates that when only the magnetic field is applied, the pinning events are significantly more prominent compared to the thin film with 1% anisotropy disorder under the same conditions. In fact, the DW remains pinned even with a field strength of 1 mT, indicating a higher depinning field in thin films with increased anisotropy disorder. The DW motion exhibits distinct characteristics depending on the frequency of the applied SAWs. As shown in Fig. 3(c), compared to the case without SAWs, the overall trend of the DW motion is enhancement in the presence of SAWs within the studied frequency range. However, the frequency of the SAW significantly influences the DW motion. Figure 3(d) illustrates the DW displacement in the thin film with 3% anisotropy disorder at 0.5 mT with and without SAWs. Without SAWs, the DW hardly moves. In contrast, the presence of 50 MHz SAWs leads to observable DW motion with a few pinning events. For example, the DW becomes pinned during the initial 10 ns, followed by motion for a short period until the next pinning event at 20 ns. With an increase in SAW frequency to 100 MHz, more significant DW motion is observed, accompanied by additional pinning events. Notably, when the SAW frequency reaches 200 MHz, continuous DW motion with minimal pinning effects occurs [as indicated by the dashed line in Fig. 3(d)]. In fact, even at 0 mT, 200 MHz SAWs facilitate the DW depinning process, while 50 MHz SAWs exhibit limited effects on DW motion, even at 1 mT. These observations suggest that SAWs with higher frequencies exert a stronger influence on DW motion in thin films with higher levels of anisotropy disorder. It is worth noting that the DW velocity, even in the presence of SAWs, is slower compared to the thin film with lower anisotropy disorder. This is attributed to the higher energy required to depin the DW in thin films with increased anisotropy disorder.

In the presence of SAWs ranging from 50 to 200 MHz, the DW motion in thin films with both 1% and 3% anisotropy disorder adheres to the creep law, as depicted in Fig. 7. Further details are given in the Appendix.

To gain insight into the DW depinning process, we examine the magnetization configuration under the influence of the magnetic field alone and in the presence of SAWs. At 10 ns into the simulation, the magnetization configuration is captured and presented in Figs. 4(a)–4(d). In the thin film with 1% anisotropy disorder and without SAWs at 0.5 mT, the DW moves steadily and coherently while maintaining its structure. A smooth DW with no significant curvature is observed, depicted as a light green line separating the left and right domains in Fig. 4(a). However, in the presence of SAWs, the DW exhibits curvatures and Bloch segments with opposite orientation (up/down) separated by VBLs as shown in Fig. 4(b). The different colored sections indicate the introduction of additional spin configurations in the wall structure induced by the SAWs [16,18,19].

In our simulations, the DW exhibits a Bloch wall structure, where the magnetization is primarily oriented in the “up” or “down” direction (along the y axis). The VBLs in our system, on the other hand, are oriented in the “left” or “right” direction

(along the x axis). Thus, the additional spin structures introduced by the VBLs can be represented by the magnetization component along the x axis (m_x). It is important to note that the "number of VBLs" in this study is not an absolute quantity; rather, we utilize m_x as a representation of the presence and density of VBLs within the system. The number of VBLs is plotted against simulation time in Figs. 4(e) and 4(f). In the thin film with 1% anisotropy disorder and the application of the magnetic field alone, the number of VBLs shows minimal change, indicating rare occurrence of spin rotations [inset graph in Fig. 4(e)]. However, when SAWs are applied, the number of VBLs exhibits periodic fluctuations, as shown in Fig. 4(e). The period of these fluctuations corresponds to the frequencies of the applied SAWs. For instance, SAWs with frequencies of 50, 100, and 200 MHz exhibit periodicities of approximately 20, 10, and 5 ns, respectively. The periodic variation in the number of VBLs with the SAW frequency arises from the magnetoelastic coupling effect. When SAWs are applied, strain is introduced to the magnetic thin film, resulting in the emergence of an effective magnetic field. This effective magnetic field plays a crucial role in both the nucleation and annihilation of VBLs, as well as influencing the motion of the DW and the VBLs within the DW, contributing to their dynamics.

In the magnetization configuration of the thin film with 3% anisotropy disorder at 0.5 mT, the DW exhibits greater curvatures [see Fig. 4(c)] and a larger number of VBLs [see Fig. 4(f)] compared to the thin film with 1% anisotropy disorder under the same conditions. The inset graphs in Figs. 4(e) and 4(f) (same scale) provide a closer look at the number of VBLs when only the magnetic field is applied within the range of 60 to 80 ns. The ensemble spread of VBLs in the thin film with 3% anisotropy disorder is approximately 2.5 times wider than that in the thin film with 1% anisotropy disorder, indicating a greater occurrence of spin rotations within the DW in the thin film with 3% anisotropy disorder. This can be attributed to the fact that the magnetic field alone is strong enough to induce DW motion and maintain DW structure in the thin film with 1% anisotropy disorder, thereby avoiding the significant formation of VBLs. However, in the thin film with 3% anisotropy disorder, the magnetic field is insufficient to enable the DW to overcome the local energy potential [19]. Consequently, the magnetic field introduces spin rotations within the DW, contributing to the broader ensemble spread of VBLs. Similar to the DW in the thin film with 1% anisotropy disorder, the number of VBLs in the thin film with 3% anisotropy disorder also undergoes periodic changes with the SAW frequency. The fluctuation behavior of VBLs in relation to the SAW frequencies is observed consistently across thin films and various applied fields.

The introduction of SAWs induces spin rotation in the DW, resulting in a smoothing of the energy landscape within the thin film. This phenomenon leads to enhanced DW motion. It is instructive to compare the effect of SAWs with the effect of thermal fluctuations on DW motion. To do this, we separately examine the effects of SAWs and temperature on DW motion [47,48]. Figure 5(a) displays the time evolution of the DW at both 0 K and 300 K in a thin film with 3% anisotropy disorder. In the absence of SAWs, the presence of thermal fluctuations at 300 K significantly enhances DW motion compared to the

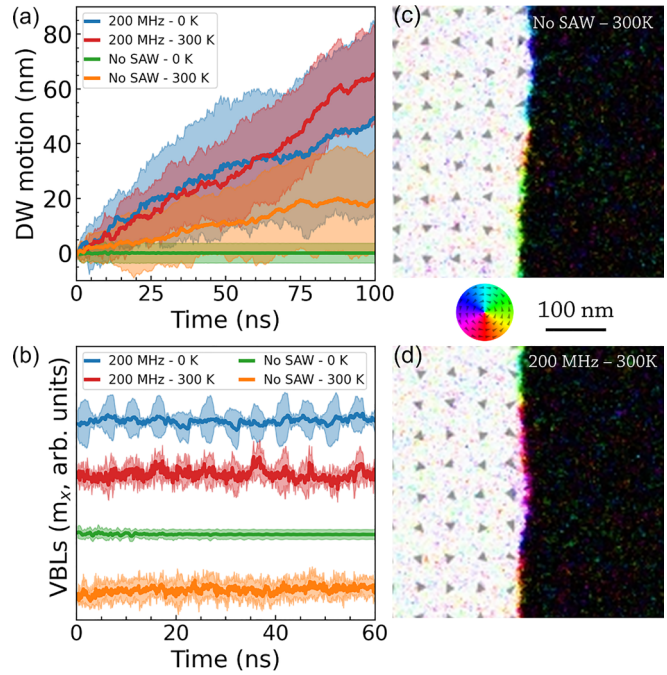

FIG. 5. (a) DW motion and (b) VBLs plotted against simulation time both without SAWs and with 200 MHz SAWs at 0 and 300 K. Snapshot of the magnetization configuration at 300 K at 10 ns (c) without SAWs and (d) with 200 MHz SAWs. The simulations are conducted in the thin film with 3% disorder under an applied field of 0.6 mT. The color code for the in-plane magnetization component is shown by a color wheel. Shaded areas indicate the ensemble spread of 10 simulations. The number of VBLs (y axis) is shifted for clarity of changes.

motion observed at 0 K. This enhancement is also evident through the presence of multiple VBLs at 300 K, as depicted in Fig. 5(c), and the variation in the number of VBLs over time, illustrated in Fig. 5(b). The number of VBLs is notably higher than in simulations conducted at 0 K without SAWs, although the changes in the number of VBLs occur randomly over time. In the presence of 200 MHz SAWs at 300 K, the DW also contains multiple VBLs, as shown in Fig. 5(d). However, in this case, the changes in the number of VBLs over time have a periodicity that aligns with the SAW frequency. Moreover, there is an additional level of randomness introduced by thermal fluctuations when compared to the scenario with 200 MHz SAWs at 0 K, as depicted in Fig. 5(c). The introduction of SAWs in magnetic thin films creates an effective field with the same periodicity as the SAW frequency. This effective field induces spin rotation, leading to the formation of VBLs within the DW. The spin rotation caused by SAWs enhances the possibility of DW depinning by smoothing the energy landscape of the thin films, similar to the effect of thermal fluctuation [47]. It is important to note that the spin rotation induced by SAWs exhibits the same frequency as the SAW, in contrast to the randomly distributed nature of thermal fluctuation. This coherent spin rotation induced by SAWs introduces a more controlled and synchronized influence on the DW dynamics, offering potential advantages for precise manipulation and control of DW motion in magnetic thin films.

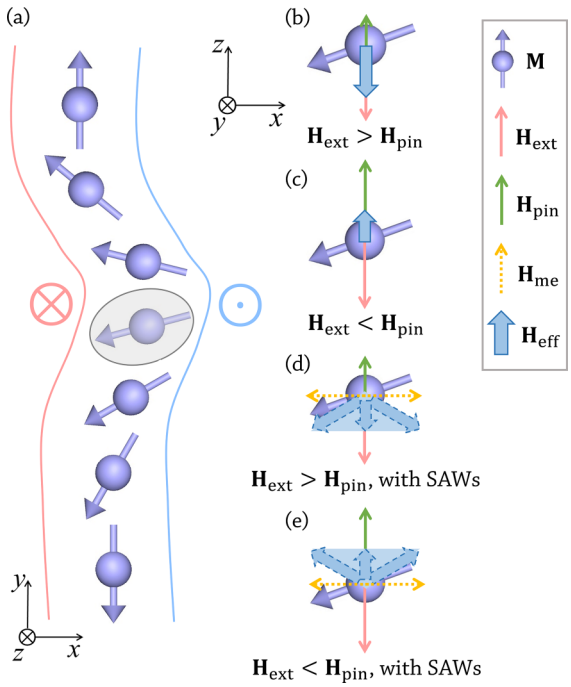

FIG. 6. (a) The left and right domains are pointing "in" and "out" of the paper, respectively, separated by a DW with VBLs. The circled spin is used to analyze the effective fields under different conditions in (b)–(e). (b) $\mathbf{H}_{ext} > \mathbf{H}_{pin}$ without SAW. (c) $\mathbf{H}_{ext} < \mathbf{H}_{pin}$ without SAW. (d) $\mathbf{H}_{ext} > \mathbf{H}_{pin}$ with SAWs. (e) $\mathbf{H}_{ext} > \mathbf{H}_{pin}$ with SAWs.

The SAW-induced effective field and spin rotation, are critical in modulating the local energy landscape. Figure 6(a) shows a schematic of a DW containing a VBL with a curvature separating the left and right domain. Note that only external magnetic field ($\mathbf{H}_{ext}$) and effective fields generated by pinning potential ($\mathbf{H}_{pin}$) and SAWs ($\mathbf{H}_{me}$) are demonstrated in the sketch. When only external magnetic field applied is applied and no SAW, the magnetic moment mainly experiences two torques generated by external magnetic field and local effective pinning field, respectively. In the simulation, the pinning is introduced by the magnetic anisotropy in out-of-plane direction (K_u). Therefore, only pinning in the z axis is taken into consideration. When $\mathbf{H}_{ext}$ is larger than $\mathbf{H}_{pin}$ [as shown in Fig. 6(b)], the magnetic moment aligns to the net effective field resulting in the DW motion towards the right. However, when $\mathbf{H}_{ext}$ is smaller than $\mathbf{H}_{pin}$ [as shown in Fig. 6(c)], the DW is pinned at the local pinning site since the net effective field is smaller than the local effective pinning field. Owing to the magnetoelastic coupling effect, the dynamic strain induced by SAWs generates a dynamic effective field [as shown in Figs. 6(d) and 6(e)]. This effective field exerts an extra dynamic torque on the magnetic moment within the DW (in our simulation, only in-plane strain is taken into consideration). The SAW-induced dynamic effective field can promote diverse spin configurations within the DW (as evidenced by the formation of VBLs). Under certain configurations together with other effective fields (such as exchange interaction), the DW can overcome these local energy barriers. Hence, SAWs not only generate an effective field for DW motion but also induce spin rotations and VBLs, facilitating the most conducive spin configurations for DW depinning.

The SAW-induced spin rotation has two distinct effects on DW motion: (i) The spin rotation increases the likelihood of DW depinning from pinning sites, thereby promoting DW motion. (ii) The spin rotation leads to energy dissipation at the DW, resulting in SAW energy loss. These two effects have contrasting consequences on DW motion. On one hand, they can increase the DW velocity by enhancing the probability of depinning. On the other hand, the energy dissipation can limit the amount of SAW energy available to enhance DW motion. Higher SAW frequencies correspond to higher spin rotation frequencies, which, in turn, lead to increased energy dissipation of the SAW. In the thin film with 3% disorder, the effect (i) is more significant, resulting in enhanced DW velocity and depinning with increasing SAW frequency. In contrast, the thin film with 1% disorder experiences a greater impact from effect (ii), leading to a smaller DW velocity in the presence of SAWs with higher frequencies. At low magnetic fields, material defects or grain boundaries act as potential wells, serving as pinning sites for the motion of the DW [11,13,16]. SAWs in our thin films introduce energy fluctuations with the same frequency as the SAWs, which promote the depinning of the DW from these pinning sites [38,48,49].

IV. CONCLUSIONS

In summary, our study investigated the impact of SAW frequency (50, 100, and 200 MHz) on the DW motion in thin films with different levels of anisotropy disorder through micromagnetic simulations. The results demonstrated that SAWs enhance DW velocity by promoting the depinning of DWs from pinning sites through SAW-induced spin rotation, which was consistently observed across all cases studied. The spin rotation not only increases the likelihood of DW depinning but also contributes to SAW energy dissipation. In the thin film with 3% anisotropy disorder, the DW velocity increases with the rise in SAW frequency, primarily due to the amplifying effect of spin rotation, which enhances the probability of DW depinning. Conversely, in the thin film with 1% anisotropy disorder, the DW velocity decreases with increasing SAW frequency due to the significant SAW-induced spin rotation, leading to pronounced SAW energy dissipation as the primary factor influencing DW motion. These findings provide valuable insights into the intricate interplay between SAWs, spin rotation, and DW dynamics, highlighting the crucial role of anisotropy disorder in governing the response of DWs to SAWs.

The data that support the findings are available in the University of Leeds at [50].

ACKNOWLEDGMENTS

The authors gratefully acknowledge funding from the European Union's Horizon 2020 research and innovation programme under the Marie Skłodowska-Curie Grant Agreement No. 860060, "Magnetism and the effect of Electric

Field" (MagnEFi). J.E. Cunningham gratefully acknowledges funding from EPSRC (Grants No. EP/V004743/1, No. EP/V047914/1, and No. EP/W028921/1).

The authors have no conflicts to disclose.

APPENDIX: DOMAIN WALL CREEP MOTION

The velocity of DW creep motion can be expressed as [11–13,51]

$$v = v_0 \exp\left(-\alpha H_{ext}^{-1/4}\right), \tag{A1}$$

where v_0 is a velocity scaling parameter [11,52] and the energy barrier scaling parameter α can be written as

$$\alpha = \frac{U_c}{k_B T} H_{dep}^{1/4}, \tag{A2}$$

where U_c represents the pinning energy barrier resulting from a disordered energy landscape, k_B is Boltzmann's constant, H_{ext} is the applied external magnetic field, and H_{dep} is the depinning field.

The application of SAWs has an effect on both U_c and H_{dep}, thus α is a better measure of how SAWs affect the DW motion. A smaller α represents a smoother energy landscape [51]. Figure 7 shows the natural logarithm of DW velocity ($\ln v$) plotted against $H^{-1/4}$ for thin films with 1% and 3% anisotropy disorder, influenced by SAWs spanning from 50 to 200 MHz. H is plotted within 0.4 to 1 mT, as the DW motion in the absence of the SAWs is negligible under 0.4 mT for the thin film with 1% anisotropy disorder [as shown in Fig. 2(b)]. Given the observed linearity when subject to Eq. (A1) in the studied magnetic field range [Figs. 7(a)–7(g)], it is possible that the DW motion in the presence of the SAW might be consistent with the characteristics of the creep regime. However, in the case of thin film with 3% anisotropy disorder without SAW, DW hardly moves within the applied field of 0 to 1 mT [as shown in Fig. 2(c)], therefore, the creep law does not apply [see Fig. 7(h)]. It is important to highlight that

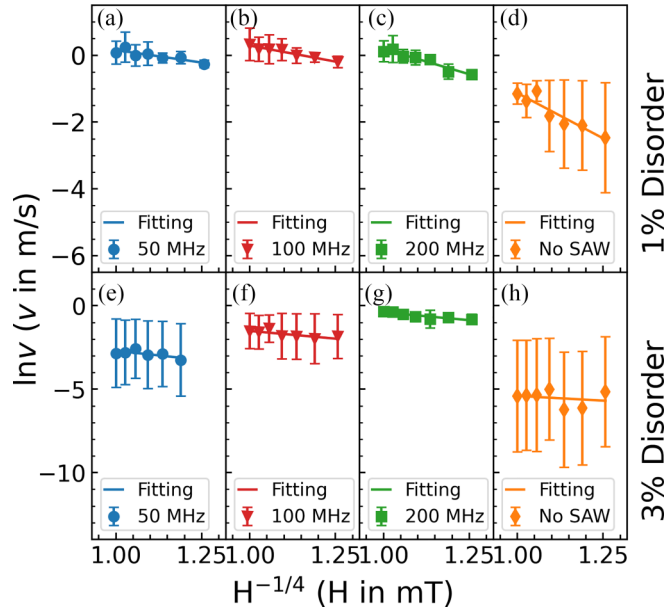

FIG. 7. Plot of the natural logarithm of DW velocity ($\ln v$) against $H^{-1/4}$. Displayed data is for thin films under varying conditions. [(a)–(d)] Thin film with 1% anisotropy disorder subjected to SAWs at 50 MHz, 100 MHz, 200 MHz, and no SAW, respectively. [(f)–(g)] Thin film with 3% anisotropy disorder subjected to SAWs at 50 MHz, 100 MHz, 200 MHz, and no SAW, respectively. Error bars represent the ensemble spread of 10 simulations. The solid lines are linear fitting of the simulation results against Eq. (A1).

Eq. (A1) represents the conventional creep model. This model was initially formulated for a static effective magnetic field. In the context of our study, the SAW assists the DW motion by introducing a dynamic effective field. Therefore, adjustments to the standard creep model may be necessary to account for this dynamic influence.

The presence of the SAW smooths out the energy landscape, resulting in a faster DW motion. As evidence, in the thin film exhibiting 1% disorder, the α value changes from $5.4 \pm 0.9\,\mathrm{mT}^{1/4}$ (without SAWs) to $1.5 \pm 0.4\,\mathrm{mT}^{1/4}$ with the presence of 50 MHz SAWs [Fig. 7(a)].

[1] S. S. P. Parkin, M. Hayashi, and L. Thomas, Magnetic domain-wall racetrack memory, Science **320**, 190 (2008).

[2] L. Herrera Diez, F. García-Sánchez, J.-P. Adam, T. Devolder, S. Eimer, M. S. El Hadri, A. Lamperti, R. Mantovan, B. Ocker, and D. Ravelosona, Controlling magnetic domain wall motion in the creep regime in He+-irradiated CoFeB/MgO films with perpendicular anisotropy, Appl. Phys. Lett. **107**, 032401 (2015).

[3] I. M. Miron, T. Moore, H. Szambolics, L. D. Buda-Prejbeanu, S. Auffret, B. Rodmacq, S. Pizzini, J. Vogel, M. Bonfim, A. Schuhl *et al.*, Fast current-induced domain-wall motion controlled by the Rashba effect, Nat. Mater. **10**, 419 (2011).

[4] K.-S. Ryu, L. Thomas, S.-H. Yang, and S. Parkin, Chiral spin torque at magnetic domain walls, Nat. Nanotechnol. **8**, 527 (2013).

[5] F. Cayssol, D. Ravelosona, C. Chappert, J. Ferré, and J. P. Jamet, Domain Wall Creep in Magnetic Wires, Phys. Rev. Lett. **92**, 107202 (2004).

[6] D. Kumar, T. Jin, R. Sbiaa, M. Kläui, S. Bedanta, S. Fukami, D. Ravelosona, S.-H. Yang, X. Liu, and S. N. Piramanayagam, Domain wall memory: Physics, materials, and devices, Phys. Rep. **958**, 1 (2022).

[7] A. J. Schellekens, A. Van den Brink, J. H. Franken, H. J. M. Swagten, and B. Koopmans, Electric-field control of domain wall motion in perpendicularly magnetized materials, Nat. Commun. **3**, 847 (2012).

[8] N. L. Schryer and L. R. Walker, The motion of 180 domain walls in uniform dc magnetic fields, J. Appl. Phys. **45**, 5406 (1974).

[9] V. Jeudy, A. Mougin, S. Bustingorry, W. S. Torres, J. Gorchon, A. B. Kolton, A. Lemaître, and J.-P. Jamet, Universal Pinning Energy Barrier for Driven Domain Walls in Thin Ferromagnetic Films, Phys. Rev. Lett. **117**, 057201 (2016).

[10] J. Ferré, P. J. Metaxas, A. Mougin, J.-P. Jamet, J. Gorchon, and V. Jeudy, Universal magnetic domain wall dynamics in the presence of weak disorder, C. R. Phys. **14**, 651 (2013).

[11] P. J. Metaxas, J. P. Jamet, A. Mougin, M. Cormier, J. Ferré, V. Baltz, B. Rodmacq, B. Dieny, and R. L. Stamps, Creep and Flow Regimes of Magnetic Domain-Wall Motion in Ultrathin Pt/Co/Pt Films with Perpendicular Anisotropy, Phys. Rev. Lett. **99**, 217208 (2007).

[12] P. M. Shepley, A. W. Rushforth, M. Wang, G. Burnell, and T. A. Moore, Modification of perpendicular magnetic anisotropy and domain wall velocity in Pt/Co/Pt by voltage-induced strain, Sci. Rep. **5**, 7921 (2015).

[13] P. Chauve, T. Giamarchi, and P. Le Doussal, Creep and depinning in disordered media, Phys. Rev. B **62**, 6241 (2000).

[14] C. Burrowes, N. Vernier, J.-P. Adam, L. H. Diez, K. Garcia, I. Barisic, G. Agnus, S. Eimer, J.-V. Kim, T. Devolder *et al.*, Low depinning fields in Ta-CoFeB-MgO ultrathin films with perpendicular magnetic anisotropy, Appl. Phys. Lett. **103**, 182401 (2013).

[15] A. Mougin, M. Cormier, J. P. Adam, P. J. Metaxas, and J. Ferré, Domain wall mobility, stability and walker breakdown in magnetic nanowires, Europhys. Lett. **78**, 57007 (2007).

[16] M. Voto, L. Lopez-Diaz, and L. Torres, Effects of grain size and disorder on domain wall propagation in CoFeB thin films, J. Phys. D **49**, 185001 (2016).

[17] T. Herranen and L. Laurson, Domain walls within domain walls in wide ferromagnetic strips, Phys. Rev. B **92**, 100405(R) (2015).

[18] K. Yamada and Y. Nakatani, Excitation of magnetic domain wall velocity in (Co/Ni) nanowires induced by blocking the motion of vertical Bloch lines, Appl. Phys. Express **8**, 093004 (2015).

[19] Y. Yoshimura, K.-J. Kim, T. Taniguchi, T. Tono, K. Ueda, R. Hiramatsu, T. Moriyama, K. Yamada, Y. Nakatani, and T. Ono, Soliton-like magnetic domain wall motion induced by the interfacial Dzyaloshinskii–Moriya interaction, Nat. Phys. **12**, 157 (2016).

[20] M. R. Lian and F. B. Humphrey, Observation of vertical Bloch line propagation, J. Appl. Phys. **57**, 4065 (1985).

[21] T. Herranen and L. Laurson, Bloch-line dynamics within moving domain walls in 3D ferromagnets, Phys. Rev. B **96**, 144422 (2017).

[22] W.-G. Yang and H. Schmidt, Acoustic control of magnetism toward energy-efficient applications, Appl. Phys. Rev. **8**, 021304 (2021).

[23] L. Thevenard, J.-Y. Duquesne, E. Peronne, H. J. Von Bardeleben, H. Jaffres, S. Ruttala, J.-M. George, A. Lemaître, and C. Gourdon, Irreversible magnetization switching using surface acoustic waves, Phys. Rev. B **87**, 144402 (2013).

[24] L. Thevenard, I. S. Camara, S. Majrab, M. Bernard, P. Rovillain, A. Lemaître, C. Gourdon, and J.-Y. Duquesne, Precessional magnetization switching by a surface acoustic wave, Phys. Rev. B **93**, 134430 (2016).

[25] I. S. Camara, J.-Y. Duquesne, A. Lemaître, C. Gourdon, and L. Thevenard, Field-Free Magnetization Switching by an Acoustic Wave, Phys. Rev. Appl. **11**, 014045 (2019).

[26] J. Shuai, M. Ali, L. Lopez-Diaz, J. E. Cunningham, and T. A. Moore, Local anisotropy control of Pt/Co/Ir thin film with perpendicular magnetic anisotropy by surface acoustic waves, Appl. Phys. Lett. **120**, 252402 (2022).

[27] W. Li, B. Buford, A. Jander, and P. Dhagat, Acoustically assisted magnetic recording: A new paradigm in magnetic data storage, IEEE Trans. Magn. **50**, 37 (2014).

[28] J. Dean, M. T. Bryan, J. D. Cooper, A. Virbule, J. E. Cunningham, and T. J. Hayward, A sound idea: Manipulating domain walls in magnetic nanowires using surface acoustic waves, Appl. Phys. Lett. **107**, 142405 (2015).

[29] W. Edrington, U. Singh, M. A. Dominguez, J. R. Alexander, R. Nepal, and S. Adenwalla, SAW assisted domain wall motion in Co/Pt multilayers, Appl. Phys. Lett. **112**, 052402 (2018).

[30] E. Vilkov, O. Byshevski-Konopko, P. Stremoukhov, A. Safin, M. Logunov, D. Kalyabin, S. Nikitov, and A. Kirilyuk, Magnetic domain wall motion driven by an acoustic wave, Ultrasonics **119**, 106588 (2022).

[31] Y. Wei, X. Li, R. Gao, H. Wu, X. Wang, Z. Zeng, J. Wang, and Q. Liu, Surface acoustic wave assisted domain wall motion in $[Co/Pd]_2/Pd(t)/Py$ multilayers, J. Magn. Magn. Mater. **502**, 166546 (2020).

[32] Y. Cao, X. N. Bian, Z. Yan, L. Xi, N. Lei, L. Qiao, M. S. Si, J. W. Cao, D. Z. Yang, and D. S. Xue, Surface acoustic wave-assisted spin–orbit torque switching of the Pt/Co/Ta heterostructure, Appl. Phys. Lett. **119**, 012401 (2021).

[33] J. Shuai, R. G. Hunt, T. A. Moore, and J. E. Cunningham, Separation of Heating and Magnetoelastic Coupling Effects in Surface-Acoustic-Wave-Enhanced Creep of Magnetic Domain Walls, Phys. Rev. Appl. **20**, 014002 (2023).

[34] A. Adhikari and S. Adenwalla, Surface acoustic waves increase magnetic domain wall velocity, AIP Adv. **11**, 015234 (2021).

[35] A. Adhikari, E. R. Gilroy, T. J. Hayward, and S. Adenwalla, Surface acoustic wave assisted depinning of magnetic domain walls, J. Phys.: Condens. Matter **33**, 31LT01 (2021).

[36] A. Vansteenkiste, J. Leliaert, M. Dvornik, M. Helsen, F. Garcia-Sanchez, and B. Van Waeyenberge, The design and verification of Mumax3, AIP Adv. **4**, 107133 (2014).

[37] T. Yokouchi, S. Sugimoto, B. Rana, S. Seki, N. Ogawa, S. Kasai, and Y. Otani, Creation of magnetic skyrmions by surface acoustic waves, Nat. Nanotechnol. **15**, 361 (2020).

[38] J. Leliaert, B. Van de Wiele, A. Vansteenkiste, L. Laurson, G. Durin, L. Dupré, and B. Van Waeyenberge, Current-driven domain wall mobility in polycrystalline permalloy nanowires: A numerical study, J. Appl. Phys. **115**, 233903 (2014).

[39] J. Leliaert, B. Van de Wiele, A. Vansteenkiste, L. Laurson, G. Durin, L. Dupré, and B. Van Waeyenberge, Influence of material defects on current-driven vortex domain wall mobility, Phys. Rev. B **89**, 064419 (2014).

[40] P. Kuszewski, I. S. Camara, N. Biarrotte, L. Becerra, J. von Bardeleben, W. S. Torres, A. Lemaître, C. Gourdon, J. Y. Duquesne, and L. Thevenard, Resonant magneto-acoustic switching: influence of Rayleigh wave frequency and wavevector, J. Phys.: Condens. Matter **30**, 244003 (2018).

[41] J.-V. Kim and M.-W. Yoo, Current-driven skyrmion dynamics in disordered films, Appl. Phys. Lett. **110**, 132404 (2017).

[42] F. Vanderveken, J. Mulkers, J. Leliaert, B. Van Waeyenberg, B. Sorée, O. Zografos, F. Ciubotaru, and C. Adelmann, Finite difference magnetoelastic simulator, Open Res. Europe **1**, 1 (2021).

[43] C. Campbell, *Surface Acoustic Wave Devices and Their Signal Processing Applications* (Elsevier, Amsterdam, 2012).

[44] R. Nepal, U. Güngördü, and A. A. Kovalev, Magnetic skyrmion bubble motion driven by surface acoustic waves, Appl. Phys. Lett. **112**, 112404 (2018).

[45] J. Paskauskas, R. Rimeika, and D. Ciplys, Velocity and attenuation of surface acoustic waves in proton-exchanged 128 degrees-rotated y-cut $LiNbO_3$, J. Phys. D **28**, 1419 (1995).

[46] Y. Nakatani, A. Thiaville, and J. Miltat, Faster magnetic walls in rough wires, Nat. Mater. **2**, 521 (2003).

[47] E. Martinez, L. Lopez-Diaz, L. Torres, C. Tristan, and O. Alejos, Thermal effects in domain wall motion: Micromagnetic simulations and analytical model, Phys. Rev. B **75**, 174409 (2007).

[48] J. Leliaert, B. Van de Wiele, J. Vandermeulen, A. Coene, A. Vansteenkiste, L. Laurson, G. Durin, B. Van Waeyenberge, and L. Dupré, Thermal effects on transverse domain wall dynamics in magnetic nanowires, Appl. Phys. Lett. **106**, 202401 (2015).

[49] J. Ryu, S.-B. Choe, and H.-W. Lee, Magnetic domain-wall motion in a nanowire: Depinning and creep, Phys. Rev. B **84**, 075469 (2011).

[50] J. Shuai, L. Lopez-Diaz, J. E. Cunningham, and T. A. Moore, Surface acoustic wave effect on magnetic domain wall dynamics - dataset, University of Leeds (2023), https://doi.org/10.5518/1416.

[51] P. M. Shepley, H. Tunnicliffe, K. Shahbazi, G. Burnell, and T. A. Moore, Magnetic properties, domain-wall creep motion, and the Dzyaloshinskii-Moriya interaction in Pt/Co/Ir thin films, Phys. Rev. B **97**, 134417 (2018).

[52] E. E. Ferrero, S. Bustingorry, A. B. Kolton, and A. Rosso, Numerical approaches on driven elastic interfaces in random media, C. R. Phys. **14**, 641 (2013).